

NANO EXPRESS

Open Access



# Room Temperature Crystallization of Hydroxyapatite in Porous Silicon Structures

M. Santana<sup>1,3</sup>, J. O. Estevez<sup>1\*</sup>, V. Agarwal<sup>2</sup> and R. Herrera-Becerra<sup>1</sup>

## Abstract

Porous silicon (PS) substrates, with different pore sizes and morphology, have been used to crystallize hydroxyapatite (HA) nano-fibers by an easy and economical procedure using a co-precipitation method at room temperature. In situ formation of HA nanoparticles, within the meso- and macroporous silicon structure, resulted in the formation of nanometer-sized hydroxyapatite crystals on/within the porous structure. The X-ray diffraction technique was used to determine the tetragonal structure of the crystals. Analysis/characterization demonstrates that under certain synthesis conditions, growth and crystallization of hydroxyapatite layer on/inside PS can be achieved at room temperature. Such composite structures expand the possibility of designing a new bio-composite material based on the hydroxyapatite and silicon synthesized at room temperature.

**Keywords:** Porous silicon, Hydroxyapatite, Co-precipitation method

## Background

Porous silicon is a nanostructured material obtained by electrochemical anodization of monocrystalline silicon (c-Si) in a solution of hydrofluoric acid and ethanol [1]. One of the most important characteristics of PS is its high specific surface area [1–3], which was shown to have a nanostructured fractal (self-similar) surface [4] with tunable interconnected pores. It serves as an ideal substrate for crystal growth of different materials such as proteins [5, 6], oxides [7], semiconductors [8], metallic nanoparticles [9], and hydroxyapatites [2, 10]. Moreover, heterogeneous nucleation occurs more often than homogeneous nucleation. In different studies, the pore filling via nucleation inside the pore itself or nucleation from a branching pore has been demonstrated [11]. Such fractal surface features have a great impact on the properties of different nanostructured materials adsorbed or grown over it [1–3]. The high specific surface area of porous silicon makes it highly reactive as well as biocompatible and biodegradable [1, 2]. Such characteristics provide a variety of applications such as sensors based on both electrical and optical properties, or in various

medical applications such as intelligent drug delivery in the body [1, 2], and bone implants [10].

In vitro studies, involving the immersion of various materials in simulated body fluids [12–15], have used suitable porosities of mesoporous silicon in the formation of physiologically stable hydroxyapatite on its surface [16, 17]. Additionally, it has been used as surface substrates for cell culture based on hydroxyapatite-PS [18] and intelligent implants [19]. For obtaining composites based on PS and HA, different deposition methods have been proposed [20–22]. In addition, PS can be easily integrated into conventional electronics making feasible the possibility of developing smart bio-devices based on hydroxyapatite [1–3, 23].

On the other hand, HA is the principal constituent of the bone and has been used to induce bone and teeth formation at particular biological sites requiring bone repair and crystalline growth on composite-metallic substrates [24–26]. HA is present in the mineralized tissues in the form of microscopic crystals of impure ultrastructural complexes (such as enamel), with crystal size of approximately 1  $\mu\text{m}$  long and 50 nm in diameter. As an example, in dentin and bone tissues, the HA crystal size is smaller than enamel [27]. From the dental standpoint, the crystalline orientation in the enamel is interesting due to the dissolution of the crystals in the process of cavity formation [28]. Consequently, the properties of

\* Correspondence: [jestevez@fisica.unam.mx](mailto:jestevez@fisica.unam.mx)

<sup>1</sup>Institute of Physics, UNAM, Circuito de la Investigación Científica Ciudad Universitaria, México C. P. 04510, México

Full list of author information is available at the end of the article

HA are directly influenced by particle size and morphology [29]. The influence of the preparation methods on the chemical properties of HA is crucial, mainly due to its stability in a wide range of compositions, as well as accepting a variety of anionic and cationic substitutions. As a consequence of this, its behavior as biomaterial in a composite form can be easily modified for its development in tissue engineering [30–34] and drug delivery [35–37]. As HA morphology is sensitive to the preparation conditions, obtaining HA particles with desired characteristics could be tailored by appropriate selection of the synthetic pathway and the type of substrates in which HA can grow.

In this paper, we review our experimental results on enhanced infiltration, adhesion, nucleation, and crystallization of biological and inorganic materials in meso- and macroporous silicon. The phenomena of enhanced nucleation and crystallization of biological and inorganic materials on porous silicon are explained in terms of the level of surface fractality as well as pore size and shape. The proposed method is a new way to obtain HA-PS composites at room temperature.

## Methods

### Mesoporous Silicon

Nanostructured PS was obtained by the electrochemical etching of n- and p-type, (100) oriented silicon, with a resistivity of 0.001–0.005 and 0.002–0.005  $\Omega$ -cm, respectively. To study the nucleation of HA within the n-type PS template, anodization was carried out under illumination (254 nm), with electrolyte consisting of a mixture of aqueous 48 wt.% HF (hydrofluoric acid) and absolute ethanol (99.9 %) in a volumetric ratio of 2:1, respectively. The PS layer was obtained by applying a constant current density of 80 mA/cm<sup>2</sup> for 2 min. p-type boron-doped silicon was etched at a constant current density of 70 mA/cm<sup>2</sup> for 2 min, with an electrolyte consisting of HF and ethanol in the volumetric ratio of 1:1. All the PS templates were thermally oxidized in air at 300 °C.

### Macroporous Silicon

Macroporous silicon substrates were obtained by electrochemical dissolution of low doped, 8–12  $\Omega$ -cm, (100) oriented, n-type single-side polished crystalline Si substrate. A mixture of 48 wt.% aqueous HF and absolute ethanol in volumetric ratio of 1:4 was used as electrolyte to perform the etching process for 10 min. Samples were fabricated under the influence of electric and magnetic fields applied simultaneously. Experimental configuration consisted of n-type Si substrates with ohmic contacts prepared by rubbing Ga-In eutectic at the two extreme ends of the silicon wafer (30 × 10 mm). A lateral current flow ( $I_x = 100$  mA) was applied across the Si substrate, while a platinum electrode was joined to the

negative terminal (cathode) of the applied lateral current (across the Si sample). A magnetic field  $H_y = 0.4$  T was placed perpendicular to the direction of the current ( $I_x$ ), so that the majority charge carriers (electrons,  $e^-$ ) flowing in the  $x$ -direction will be swept down by the effect of the resulting Lorentz force, leading to a major accumulation of valance band holes ( $h^+$ ) at the HF-silicon interface, promoting the reaction. On the other hand, the lateral electric field contributes to the formation of a structural gradient across the sample in terms of pore size (from approximately 3  $\mu$ m to 500 nm). The above-mentioned macroporous silicon formation process has been described in detail by Antunez et al. [38].

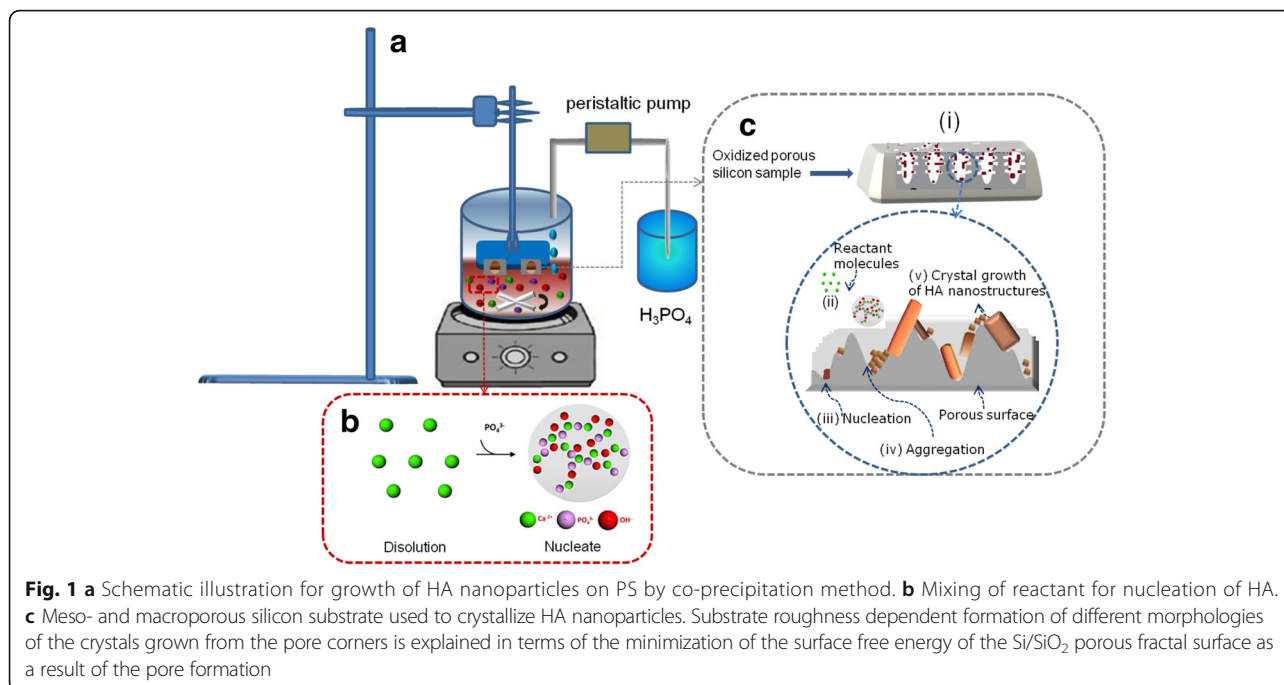
### HA Synthesis

On the other hand, HA samples were synthesized by coprecipitation method, with the following reagents: Ca(NO<sub>3</sub>)<sub>2</sub>·4H<sub>2</sub>O (Sigma-Aldrich, 99 %), N(C<sub>3</sub>H<sub>7</sub>)<sub>4</sub>OH (Sigma-Aldrich, 25 %), distilled water, and H<sub>3</sub>PO<sub>4</sub> (Sigma-Aldrich, 85 %), following the stoichiometry of the chemical reaction reported in references [29, 39]. In this work, the following solutions were prepared: tannic acid 2 %; calcium chloride dihydrate 0.2 M; phosphoric acid 0.12 M; tetrapropyl ammonium hydroxide 0.2 M, and calcium nitrate tetrahydrate 0.2 M. The phosphoric acid was adjusted to pH 9 with tetrapropyl ammonium hydroxide via a gradual process. Aqueous solutions were prepared, mixed with constant stirring of 300 rpm, and reduced. The HA was synthesized in aqueous solution and was subsequently dried by a freeze-drying technique to obtain a powder as a final product (denoted as HA powder sample).

For obtaining the composite HA@PS-n, HA@PS-p and MPS-HA, samples were immersed vertically in a solution containing the abovementioned precursors (schematically shown in Fig. 1a). The HA precursor solution kept in contact with the bottom half of the porous layer and infiltrates in the upper half by capillarity throughout the porous structure. Although the bottom part of the PS template is fractured due to the constant stirring for 24 h, the well-structured composite is formed within/over the upper half of the PS template through capillary action of the precursor solutions. Subsequently the sample obtained in aqueous solution is washed three times with a mixture of methanol-distilled water (1:2). The porous silicon-HA composite is washed with a dilute solution of methanol for further characterization.

### Characterization

The synthesized powders, HA@PS and MPS-HA samples were characterized by different techniques. X-ray diffraction (XRD) analysis was performed using a Bruker AXS D8 Advance diffractometer, with CuK $\alpha$  radiation ( $2\theta$  from 4° to 110° with a step of 0.019°). Raman



spectroscopy (Thermo Scientific) with confocal microscope and a 532-nm laser excitation source (10 mW) was used to measure the functional groups in the range of 3000–50 cm<sup>-1</sup>. For further analysis of structure and crystallinity, transmission electron microscopy (TEM) of HA powders was performed through a JEOL JEM-2010F FasTem. Finally, the high-resolution scanning electron microscopy (HRSEM) JEOL JSM-7800F was used to analyze the morphology of the composite templates and to obtain EDS maps (on MPS-HA sample).

## Results and Discussion

The chemical composition of hexagonal HA (within the ideal P6<sub>3</sub>/m space group) is Ca(I)<sub>4</sub>Ca(II)<sub>6</sub>(PO<sub>4</sub>)<sub>6</sub>(OH)<sub>2</sub> [29]. The Ca(I) site is surrounded by six PO<sub>4</sub><sup>3-</sup> tetrahedral and coordinated by nine oxygen ions. The Ca(II) site is seven-coordinated with six oxygen ions from PO<sub>4</sub><sup>3-</sup> and one oxygen ion from OH<sup>-</sup>. In order to determine the effect of pore size on the growth and crystallization of HA nanostructures, we compare their deposition on/inside the two morphologically different nanostructured PS templates (n-, p-type) using a co-precipitation method. A schematic description of the mechanism that controls the morphology and size of HA nanostructures, due to the confinement of HAP precursor solution within the porous structure, is presented in Fig. 1b. On the basis of experimental observations, the growth processes on/within porous structures have been proposed (Fig. 1c(i)), i.e., the HA precipitation mechanism follows a series of events such as infiltration by capillarity (Fig. 1c(ii)), nucleation of the crystals on the rough

porous template (Fig. 1c(iii)), followed by aggregation induced by capillary confined Ca<sup>2+</sup> ions (Fig. 1c(iv)), and their corresponding growth (Fig. 1c(v)). The aggregation plays a highly relevant role in determining the final shape and size of HA particles [29]. As a consequence, the oriented attachment of HA grown with a regular flake-like shape (see Fig. 1c) can be observed. The above discussion reveals the significant role played by the nanostructured PS in the modification of particle size and morphology due to the confinement of the precursor solution.

## HA Powder Sample

The HA powder obtained from co-precipitation during the synthesis (not attached to porous template) was analyzed by XRD and Raman spectroscopy, and its morphology/crystalline structure was determined by TEM. Figure 2a shows the XRD spectrum of the HA powder sample obtained with the method discussed above. Diffractogram shows well-defined HA peaks revealing its polycrystalline nature. The main diffraction peaks are in good agreement with the ICDD, PDF # 01072-1243 card and in conformity with the previously reported studies using different synthesis methods [40–42]. Indexed peaks correspond to the space group P6<sub>3</sub>/m of the hexagonal phase, consistent with the already reported work at around 100 °C [29]. Diffraction peaks in the present case are found to be relatively broader, which indicates smaller particle size.

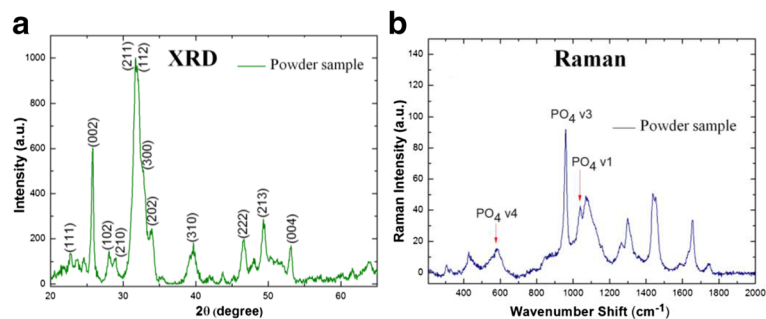


**Fig. 2** a XRD and b Raman spectra of HA powder sample

Hydroxyapatite Raman vibrations are associated with the well-known internal four different tetragonal  $\text{PO}_4^{3-}$  vibrational modes:  $\nu_1$  correspond to a totally symmetric stretching mode of the tetrahedral  $\text{PO}_4^{3-}$  group (P-O bond),  $\nu_2$  is a doubly degenerate bending mode of the phosphate group (P-O-P bond),  $\nu_3$  is a triply degenerate asymmetric stretching mode of the tetrahedral  $\text{PO}_4^{3-}$  group (P-O bond), and  $\nu_4$  is a triply degenerate bending mode of the  $\text{PO}_4$  group (O-P-O) [40, 41]. Figure 2b shows Raman spectra obtained from the HA powder sample. Three vibrational modes can be clearly identified. The analysis reveals a first band at  $1045\text{ cm}^{-1}$  corresponding to the  $\nu_3$  phosphate ( $\text{PO}_4$ ) mode. Another appears at  $958\text{ cm}^{-1}$ , corresponding to the  $\nu_1$  phosphate ( $\text{PO}_4$ ) mode, and finally one more is revealed at  $583\text{ cm}^{-1}$ , which corresponds to the typical  $\nu_4$  band ( $\text{PO}_4$ ) of hydroxyapatite [43–45].

In order to identify the morphology and particle size of HA powder sample, Fig. 3a, b shows the low- and high-magnification TEM images, respectively. Figure 3b reveals the lattice fringes used to determine the interplanar distance. Measured lattice spacing of 3.170 and 4.084 nm is found to be in agreement with the already reported spacing (corresponding to HA structure) of (102) and (200) planes, respectively. Crystal lattice parameters from the analysis of high-resolution images were found to be in agreement with those reported in the ICDD PDF # 01-072-1243 card. These results are consistent with the observed XRD analysis, shown in Fig. 2a.

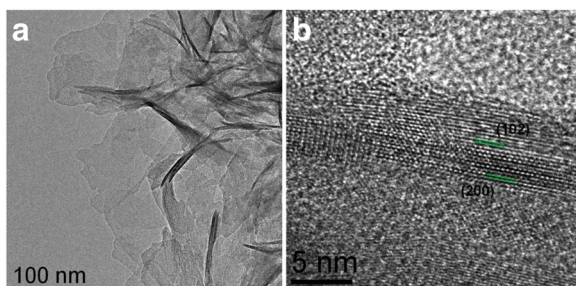


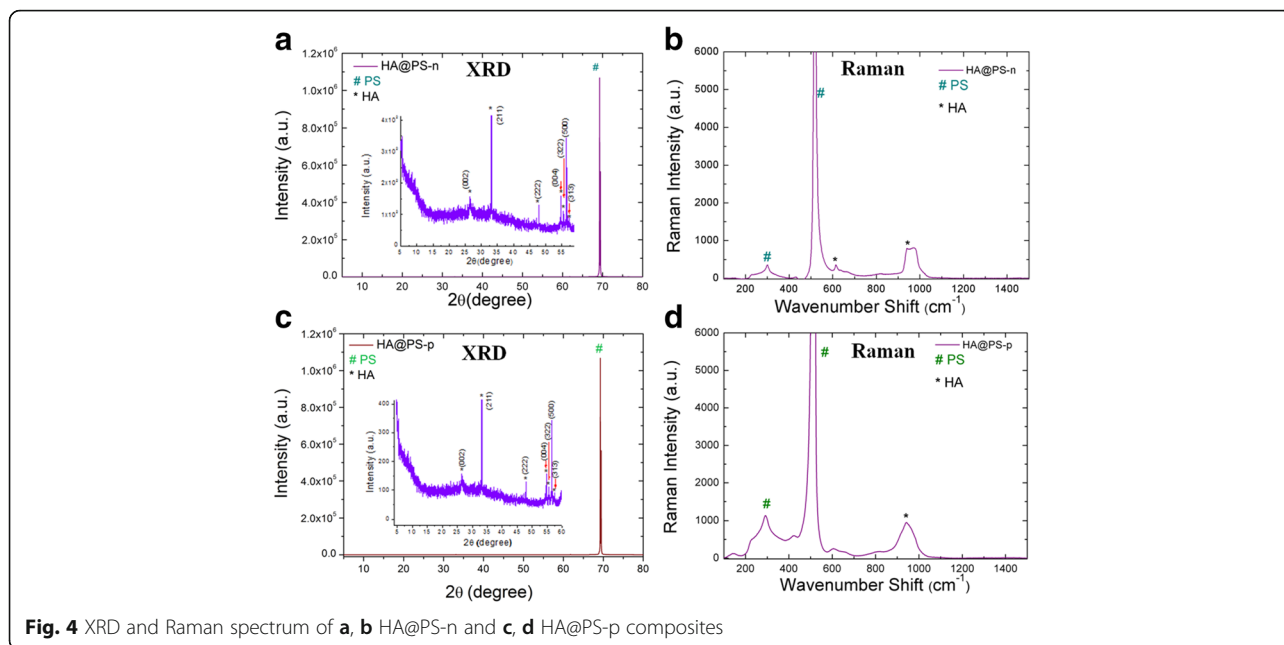
**Fig. 3** a TEM and b HRTEM images of HA obtained in powder

### Mesoporous HA@PS-n and HA@PS-p Composite Samples

In the case of mesoporous silicon composites, two different PS substrates were used to induce the nucleation of HA crystals from co-precipitation method and to show the possible HA deposition/crystallization process at room temperature. In Fig. 4, the single XRD and micro-Raman study for the HA@PS-n (Fig. 4a, b) and HA@PS-p (Fig. 4c, d) samples is presented. In both cases, the observed diffraction peaks (see Fig. 4a, c) clearly show the formation of the HA nanoparticles, in agreement with the corresponding PDF # 01072-1243 card. According to these data, the main peaks, characteristic for the HA, were the isolated (002) planes, with a peak at  $2\theta = 26^\circ$  and a broad peak, centered at  $32.5^\circ$ , which was an envelope of overlapping different (211), (112), (300), and (202) crystalline planes [21]. As the size of the individual crystal is less than 100 nm with many nanometric and randomly orientated crystals, X-ray signal shows broadening. Besides the HA crystalline phase, the sample reveals a characteristic silicon peak at  $2\theta = 69^\circ$ .

Typical vibrational modes present in HA@PS-n and HA@PS-p samples are shown in Fig. 4b, d. Two groups of peaks at about  $430$  and  $585\text{--}611\text{ cm}^{-1}$  were identified as  $\nu_2$  and  $\nu_4$  phosphate modes, characteristic of HA nanostructures. A peak at  $961\text{ cm}^{-1}$ , clearly detected in the samples HA@PS-n and HA@PS-p, was assigned to the  $\nu_1$  phosphate symmetric stretching of the HA, which is generally the strongest peak in the HA spectrum. The peaks measured at  $520$  and  $303.6\text{ cm}^{-1}$  were also assigned to crystalline silicon [21]. Similar to XRD results, this analysis confirmed the room temperature crystallization of HA on porous silicon.

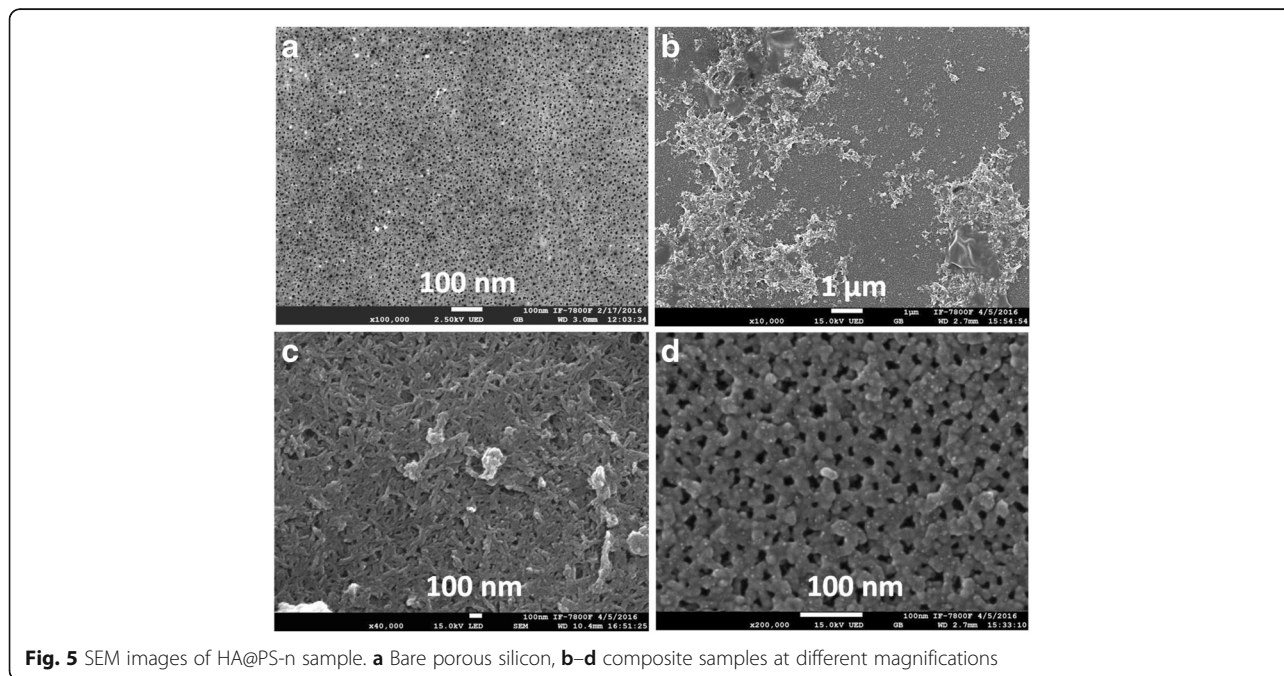
The SEM images corresponding to HA@PS-n sample obtained by electrochemical etching are shown in Fig. 5. Figure 5a shows the top view of bare n-type porous silicon substrate. Figure 5b shows the HA nucleation and agglomeration in some parts of the porous template, formed by co-precipitation method, reaching a height of approximately  $1\text{ }\mu\text{m}$  with respect to the PS surface. Due to small pore sizes (2 to 10 nm) of the PS surface, a complete infiltration within the porous silicon matrix



was not obtained. Besides, the image of Fig. 5c shows that the HA particles are floccule-like, around 50 nm in diameter, and in some areas, the particles are well-agglomerated in clusters. Morphologically, the HA particle growth in/over PS is similar to others synthesized previously [20]. Due to increased porosity in the area where the sample is in contact with the precursor solution, the growth of hydroxyapatite is very different compared to the area where the solution is infiltrated by

capillarity (see Fig. 5d). This indicates that the coprecipitation technique is viable to form a composite based on HA and PS at room temperature.

Although HRSEM images of the HA@PS-p show similar morphology as compared to HA@PS-n sample, due to the difference in the porosity of the porous template, the nucleation into the pores is relatively more efficient than p-type porous structure. Figure 6a shows the surface view of bare p-type PS substrate. Figure 6b shows



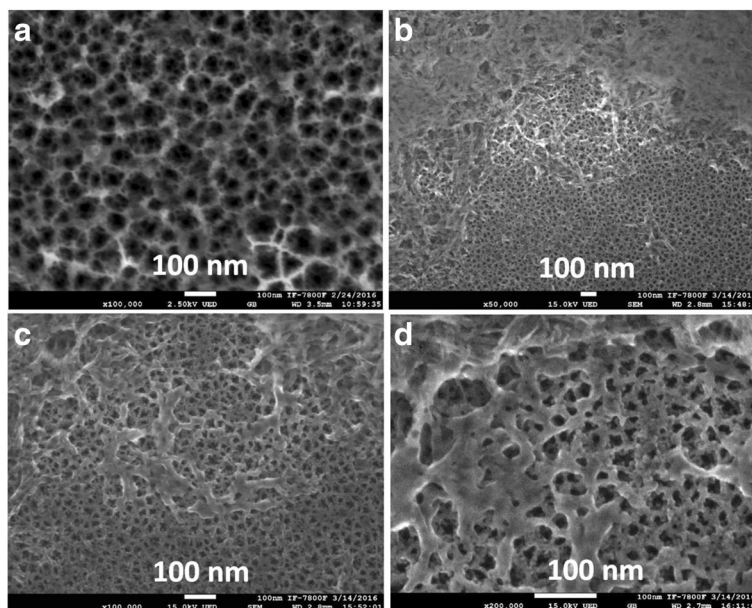


**Fig. 6** SEM images of HA@PS-p sample. **a** Bare porous silicon, **b-d** composite samples at different magnifications

that the HA nucleation formed by co-precipitation method consists of agglomerates, in some parts of sample, reaching a height of approximately 2  $\mu\text{m}$  with respect to the PS surface. Due to macropore sizes (50–100 nm) on PS surface, a partial infiltration within the porous silicon matrix was obtained. Besides, the image of Fig. 6c shows that the HA particles are interconnected fibers, around 100 nm in thickness, and in some areas into the porous template, the particles are well-agglomerated in small clusters (see Fig. 6d) of approximately 20 nm.

Figure 7 shows the single XRD and micro-Raman (Fig. 7a, b) study for the composites formed with macroporous (sample denoted as MPS-HA) silicon substrates. Similar to the HA formed over the mesoporous substrate (HA@PS-n and HA@PS-p), diffraction and

Raman [21, 39] peaks in the MPS-HA composite clearly show the presence of HA nanostructures.

In order to observe the HA nucleation in different pore dimensions in MPS structures, n-type graded macropores were fabricated employing an experimental setup which involves the simultaneous application of an electric and magnetic field along with an auxiliary metal electrode electrically connected to the negative contact of the lateral electric field (cathode) applied onto Si substrate [6, 38]. This configuration leads to the formation of linear gradient in pore size and thickness. Depending on the dimensions, the pore corners and walls of MPS structures reveal the formation of HA nanostructures of different sizes and structural shapes (Fig. 8a, b). In the present case, crystals formed within the pores are also confined due to pore size; however, they also grown

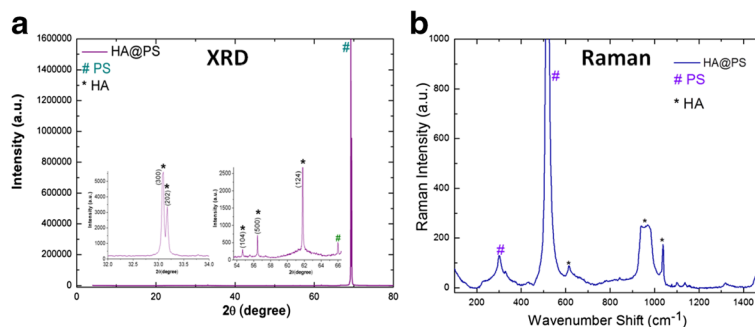


**Fig. 7** **a** XRD and **b** Raman spectra of HA@macroPS-n structure

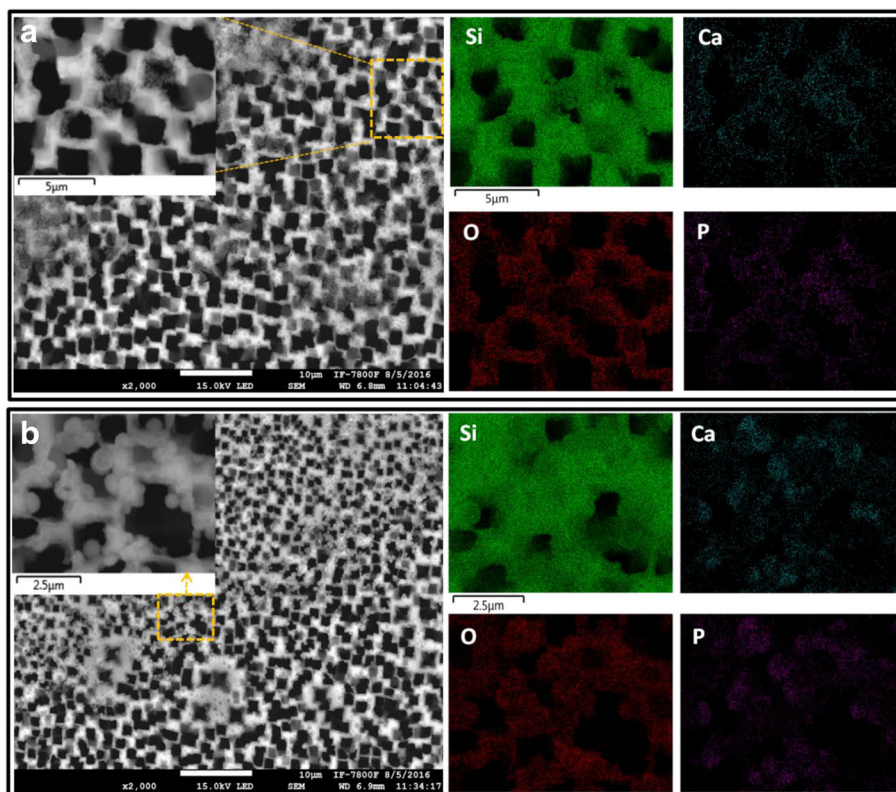


**Fig. 8** **a** High porosity zone of MPS-HA composite structure: (*left hand side*) top view taken from scanning electron microscopy (*inset* shows the magnified view); (*right hand side*) EDS mapping corresponding to the fibrous morphology confirms the nucleation and formation of HA within/over the MPS substrate. **b** Low porosity zone of MPS-HA composite structure: (*left hand side*) top view taken from scanning electron microscopy (*inset* shows the magnified view with the spherical morphology); (*right hand side*) EDS mapping corresponding to the spherical morphology confirms pore size and type the nucleation and formation of typical HA within/over the MPS substrate

from nanometer scale to typical spherical micrometric agglomerates [inset, Fig. 8b]. Different forms of agglomerations have been attributed to the different degree of surface roughness responsible for the nucleation of HA.

## Conclusions

Room temperature growth and crystallization of HA nanoparticles in/over partially oxidized porous silicon substrates have been demonstrated by co-precipitation method. Raman and XRD analyses of the composite samples revealed the characteristic phosphate peaks and the polycrystalline nature, respectively. Shape and pore size were favorable for the adhesion and growth of HA in porous structure, and the analysis confirms hydroxyapatite nanoparticles have a hexagonal structure. PS with different tunable optical and electrical properties can be used for the development of optical/electrical biosensors for monitoring HA growth. This opens the possibility to develop composite biomaterials for biomedical applications at room temperature or physiological temperature based on hydroxyapatite nanocompounds.

## Acknowledgements

The authors thank Carlos Magaña (IF-UNAM) for HRSEM, Roberto Hernández Reyes (IF-UNAM) for HRSEM images, and Antonio Morales (IF-UNAM) for the XRD patterns.

## Funding

The project has been partially supported by CONACYT (CIAM 188657), Mexico. DGAPA with grant PAPIIT (IN108915).

## Authors' contributions

MS and JOE carried out the experiments. JOE, VA, and RHB conceived the study. JOE, VA, and RHB drafted the manuscript. All authors are involved in revising the manuscript. All authors read and approved the final manuscript.

## Competing interests

The authors declare that they have no competing interests.

## Author details

<sup>1</sup>Institute of Physics, UNAM, Circuito de la Investigación Científica Ciudad Universitaria, México C. P. 04510, México. <sup>2</sup>Center for Engineering and Applied Sciences (CIICAp-UAEM), Av. Universidad 1001. Col. Chamilpa, Cuernavaca, Morelos 62209, México. <sup>3</sup>Posgrado en Ciencia e Ingeniería de Materiales, Circuito de la Investigación Científica, Ciudad Universitaria, Mexico 04510, Mexico.

Received: 5 May 2016 Accepted: 22 September 2016

Published online: 10 November 2016

## References

1. Canham L (ed) (2014) Handbook of porous silicon. Springer International Publishing, Switzerland
2. Santos HA (ed) (2014) Porous silicon for biomedical applications. Woodhead Publishing Limited, UK
3. Losic D, Santos A (ed) (2015) Electrochemically engineered nanoporous materials methods, properties and applications. Springer International Publishing, Switzerland
4. Stolyarova S, Baskin E, Nemirovsky Y (2012) Enhanced crystallization on porous silicon: facts and models. *J Cryst Growth* 360:131–133
5. Khushid S, Saridakis E, Govada L, Chayen NE (2015) Porous nucleating agents for protein crystallization. *Nat Protoc* 9:1621–1633
6. Salazar-Kuri U, Estevez JO, Antunez EE, Martínez-Aguila BS, Warren JB, Babak A, Cerniglia ML, Stojanoff V, Agarwal V (2015) Nucleation of Sub-micrometer protein crystals in square-shaped macroporous silicon structures. *Cryst Growth Des* 15:2801–2808
7. Antunez EE, Salazar-Kuri U, Estevez JO, Campos J, Basurto MA, Jiménez Sandoval S, Agarwal V (2015) Porous silicon-VO<sub>2</sub> based hybrids as possible optical temperature sensor: wavelength-dependent optical switching from visible to near-infrared range. *J Appl Phys* 118:134503
8. Korotcenkov G (ed) (2015) Porous silicon: from formation to applications: optoelectronics, microelectronics, and energy technology applications, CRC Press, vol 3
9. Polisski S, Goller B, Heck SC, Maier SA, Fujii M, Kovalev D (2011) Formation of metal nanoparticles in silicon nanopores: plasmon resonance studies. *Appl Phys Lett* 98:011912
10. Asanithi P (2014) Surface porosity and roughness of micro graphite film for nucleation of hydroxyapatite. *J Biomed Mater Res A*:2590–2599
11. Liu Y, Men Y, Zhang X (2012) Nucleation mechanism for vapor-to-liquid transition from substrates with nanoscale pores opened at one end. *J Chem Phys* 137(10):104701
12. Canham LT (1995) Bioactive silicon structure fabrication through nanoetching techniques. *Adv Mater* 7:1033–1037
13. Leigh C, Reeves CL, King DO, Branfield PJ, Crabb JG, Ward MCL (1996) Bioactive polycrystalline silicon. *Adv Mater* 8:850–852
14. Canham LT, Reeves CL, Loni A, Houlton MR, Newey JP, Simons AJ, Cox TI (1997) Calcium phosphate nucleation on porous silicon: factors influencing kinetics in a cellular simulated body fluids. *Thin Solid Films* 297:304–307
15. Martín-Palma RJ, Manso-Silván M, Torres-Costa V (2010) Biomedical applications of nanostructured porous silicon: a review. *J Nanophoton* 4:042502
16. Chin V, Collins BE, Sailor MJ, Bhatia SN (2001) Compatibility of primary hepatocytes with oxidized nanoporous silicon. *Adv Mater* 13:1877–1880
17. Henstock JR, Ruktanonchai UR, Canham LT, Anderson SI (2014) Porous silicon confers bioactivity to polycaprolactone composites in vitro. *J Mater Sci Mater Med* 25:1087–1097
18. Sánchez A, González J, García-Piñeres A, Montero ML (2011) Nano-hydroxyapatite colloid suspension coated on chemically modified porous silicon by cathodic bias: a suitable surface for cell culture. *Phys Status Solidi C* 8:1898–1902
19. Munir G, Koller G, Di Silvio L, Edirisinghe MJ, Bonfield W, Huang J (2011) The pathway to intelligent implants: osteoblast response to nano silicon-doped hydroxyapatite patterning. *J R Soc Interface* 8:678–688
20. Shaoqiang C, Zhu Z, Zhu J, Jian Z, Yanling S, Yu K, Wang W, Wang X, Xiao F, Luo L, Li S (2004) Hydroxyapatite coating on porous silicon substrate obtained by precipitation process. *Appl Surf Sci* 230:418–424
21. Pramatarova L, Pecheva E, Dimova MD, Presker R, Stutzmann M, Schwarz U, Kniep R (2005) A novel laser-liquid-solid interaction process for hydroxyapatite formation on porous silicon, vol 5830. *Proc. of SPIE*, Bellingham
22. Hernández-Montelongo J, Muñoz-Noval A, Torres-Costa V, Martín-Palma RJ, Manso Silvan M (2012) Cyclic calcium phosphate electrodeposition on porous silicon. *Int J Electrochem Sci* 7:1840–1851
23. Pietak AM, Reid JW, Stott MJ, Sayer M (2007) Silicon substitution in the calcium phosphate bioceramics. *Biomaterials* 28:4023–4032
24. Swetha M, Sahithi K, Moorthi A, Srinivasan N, Ramasamy K, Selvamurugan N (2010) Biocomposites containing natural polymers and hydroxyapatite for bone tissue engineering. *Int J Biol Macromol* 47:1–4
25. Forsgren J, Svahn F, Jarmar T, Engqvist H (2007) Formation and adhesion of biomimetic hydroxyapatite deposited on titanium substrates. *Acta Biomater* 3:980–984
26. Surmeneva MA, Kleinhans C, Vacun G, Kluger PJ, Schönhaar, Müller M, Hein SB, Wittmar A, Ulbricht M, Prymak O, Oehr C, Surmenev (2015) Nano-hydroxyapatite-coated metal-ceramic composite of iron-tricalcium phosphate: Improving the surface wettability, adhesion and proliferation of mesenchymal stem cells in vitro. *Colloids Surf B* 135:386–393
27. Reyes J, Brès EF (2015) Electron microscopic study of the human tooth enamel: the central dark line. *Encyclopedia of Anal Chem* 1:1–16
28. Tsuda H, Arends J (1994) Orientational micro-Raman spectroscopy on hydroxyapatite single crystals and human enamel crystallites. *J Dent Res* 73:1703–1710
29. Nagaprasad P, Pravas KP, Amita P (2010) Room temperature synthesis of highly hemocompatible Hydroxyapatite, study of their physical properties and spectroscopic correlation of particle size. *Nanoscale* 2:2631–2638
30. Baldino L, Naddeo F, Cardea S, Naddeo A, Reverchon E (2015) FEM modeling of the reinforcement mechanism of hydroxyapatite in PLLA scaffolds produced by supercritical drying, for tissue engineering applications. *Int J Biol Macromol* 51:225–236
31. Ito Y, Hasuda H, Kamitakahara M, Ohtsuki C, Tanihara M, Kang IK, Kwon H (2005) A composite of hydroxyapatite with electrospun biodegradable nanofibers as a tissue engineering material. *J Biosci Bioeng* 100:43–49
32. Zhang S, Prabhakaran MP, Qin X, Ramakrishna (2015) Biocomposite scaffolds for bone regeneration: role of chitosan and hydroxyapatite within poly-3-hydroxybutyrate-co-3-hydroxyvalerate on mechanical properties and in vitro evaluation. *J Mech Behav Biomed* 51:88–98
33. Ryu J, Ku SH, Lee M, Park CB (2011) Bone-like peptide/hydroxyapatite nanocomposites assembled with multi-level hierarchical structures. *Soft Matter* 7:7125–7568
34. Chen JD, Wang Y, Chen X (2009) In situ fabrication of nano-hydroxyapatite in a macroporous chitosan scaffold for tissue engineering. *J Biomater Sci* 20:1555–1565
35. Zhao CX, Yu L, Middelberg AP (2013) Magnetic mesoporous silica nanoparticles end-capped with hydroxyapatite for pH-responsive drug release. *J Mater Chem B* 1:4828
36. Zhao XY, Ying JZ, Chen F, Lu BQ, Wu J (2013) Nanosheet-assembled hierarchical nanostructures of hydroxyapatite: surfactant-free microwave-hydrothermal rapid synthesis, protein/DNA adsorption and pH-controlled release. *CrystEngComm* 15:206
37. Ribeiro M, Monteiro FJ, Ferraz MP (2012) Staphylococcus aureus and Staphylococcus epidermidis adhesion to nanohydroxyapatite in the presence of model proteins. *Biomed Mater* 7:045010
38. Antunez EE, Campos J, Basurto MA, Agarwal V (2014) Controlled morphology and optical properties of n-type porous silicon: effect of magnetic field and electrode-assisted LEF. *Nanos Res Let* 9(1):512
39. Santana Vázquez M, Estevez O, Ascencio-Aguirre F, Mendoza-Cruz R, Bazán-Díaz L, Zorrila C, Herrera-Becerra R (2016) Tannic acid assisted synthesis of flake-like hydroxyapatite nanostructures at room temperature. *Appl Phys A* 122:868
40. Bakan F, Laçın O, Sarac H (2013) A novel low temperature sol-gel synthesis process for thermally stable nano crystalline hydroxyapatite. *Powder Technol* 233:295–302
41. Paz A, Guadarrama D, López M, González J, Brizuela N, Aragón J (2012) A comparative study of hydroxyapatite nanoparticles synthesized by different routes. *Quim Nova* 35:1724–1727
42. Koutsopoulos S (2002) Synthesis and characterization of hydroxyapatite crystals: a review study on the analytical methods. *J Biomed Mater Res* 62:600–612
43. Nelson DG, Williamson BE (1982) Low-temperature laser Raman spectroscopy of synthetic carbonated apatites and dental enamel. *Aust J Chem* 35:715–727
44. Silva CC, Pinheiro AG, Miranda MAR, Góes JC, Sombra ASB (2003) Structural properties of hydroxyapatite obtained by mechanosynthesis. *Solid State Sci* 5:553–558
45. Li H, Ng BS, Khor KA, Cheang P, Clyne TW (2004) Raman spectroscopy determination of phases within thermal sprayed hydroxyapatite splats and subsequent in vitro dissolution examination. *Acta Mater* 52:445–453